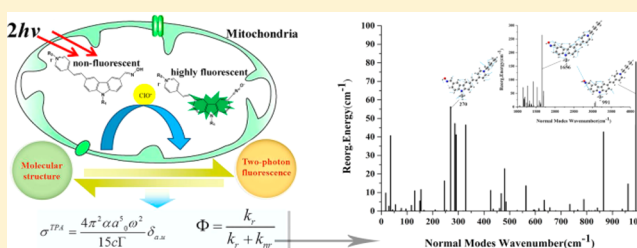


## Analyzing the Effect of Substituents on the Photophysical Properties of Carbazole-Based Two-Photon Fluorescent Probes for Hypochlorite in Mitochondria

Xue-Li Hao,<sup>†</sup> Li Zhang,<sup>†</sup> Dan Wang,<sup>†</sup> Chun Zhang,<sup>†</sup> Jing-Fu Guo,<sup>‡</sup> and Ai-Min Ren<sup>\*,†</sup><sup>†</sup>Laboratory of Theoretical and Computational Chemistry, Institute of Theoretical Chemistry, Jilin University, Liutiao Road 2#, Changchun 130061, P.R. China<sup>‡</sup>School of Physics, Northeast Normal University, Changchun 130024, P.R. China

## Supporting Information

**ABSTRACT:** The development and utilization of two-photon fluorescent probes with large two-photon absorption (TPA) cross sections ( $\delta_{\text{TPA}}$ ) and strong TP-excited fluorescence are highly needed for monitoring the level of hypochlorite in mitochondria. In this contribution, we successfully explain the fluorescence “off–on” effect observed in experiment, and clarify the fluorescent quenching mechanism of the probe containing hydroxyl oxime from the aspect of excited-state dynamics for the first time, while exploring the influence of alkyl chain length on TPA cross section and fluorescent quantum yield. It is proposed that the alkyl chain length affects significantly the fluorescent efficiency by the vibronic coupling. The proper alkyl chain length should also be one of the smart strategies for designing highly efficiency fluorescent two-photon probes applied in biological systems. We demonstrate that the designed compound HCB–CNO has exceptional optical properties, such as the larger TPA cross section (467 GM) and higher fluorescence quantum yield (0.485), compared to the experimental molecule. Moreover, the TPA tensor elements are increased remarkably by introducing strong electron-donors at the R1 position, which promote to intramolecular charge transfer, and improve significantly two-photon absorption cross sections.



## 1. INTRODUCTION

As the major source of cellular reactive oxygen species (ROS), mitochondria not only are the principal energy producing compartments in most eukaryotic cells, but they also play important roles in many biological processes including cellular differentiation, growth, and death. Hypochlorite, the key mitochondria ROS, plays essential roles in the immune system against microorganisms and inflammations.<sup>1</sup> However, an excess production of hypochlorite could give rise to many diseases such as arthritis,<sup>2</sup> atherosclerosis,<sup>3</sup> and cancers.<sup>4</sup> In order to monitor effectively the level of hypochlorite in mitochondria, many techniques for hypochlorite detection have been developed in the last years.<sup>5–14</sup> Most of them are designed on the basis of one-photon fluorescence technology. However, two-photon fluorescent probes have become more powerful tools to track mitochondria,<sup>15–17</sup> due to the advantages of the deeper penetration depth, localized excitation, and lower tissue autofluorescence in addition to reduced photon damage.<sup>18–20</sup> So far, the studies on two-photon fluorescent probes have been much less than those of single-photon fluorescence probes in both theoretical and experimental fields. The main reason is that the relationship between the molecular structures of the probes and the two-photon fluorescence is not clear, and the theoretical frame in this field is not perfect enough.<sup>5,6,21,22</sup>

Recently, Li et al. have synthesized two TP fluorescent probes (HCM and HCH) derived from carbazole core as the fluorophore and hydroxyl oxime as the recognition group.<sup>23</sup> Both of them can be applied in monitoring hypochlorite in mitochondria through oxidative dehydrogenation of oxime to the nitrile oxide. In particular, HCH shows good TPA properties, high selectivity and sensitivity, good stability, and low cytotoxicity. However, the impacts of geometric (the length of alkyl chains) and electronic structures on TPA imaging in HCM and HCH remain unclear. First, the effect of the alkyl chain length in the probe should not be underestimated due to its good compatibility with the biological systems. It is very likely to bring a new perspective for the design of excellent two-photon fluorescent probes by utilizing alkyl modification. In previous research, Wu et al. experimentally reported that the length of the terminal alkyl chain has a certain degree of influence on molecular optical performances.<sup>24</sup> Cho and his co-workers have researched the effect of chain length for membrane probes.<sup>25</sup> Nevertheless, the impact of the alkyl chain length on the two-photon nature and the fluorescent efficiency of the probe has not been thoroughly studied. Thus,

Received: November 3, 2017

Revised: January 30, 2018

Published: February 5, 2018

in-depth comprehension of the relationship between the two-photon fluorescent properties and the molecular structures is extremely urgent for the development of novel two-photon fluorescent molecules with high efficiency. Second, in many experimental and theoretical reports, one viewpoint seems to have almost been acknowledged, that is, for the probe molecules containing an unabridged C=N bond, and C=N isomerization is the predominant dissipation process of excited states leading to fluorescence quenching,<sup>26–28</sup> but which is not substantiated by sufficient evidence. Interestingly, the extremely complicated photochemical processes of the unabridged C=N bond isomerization for the probe molecules have not been involved yet. The unabridged C=N isomerization not only is affected by the circumstance and substituents easily, but it also competes with other photochemistry processes and the nonradiation decay processes which proceed by paths associated with photophysical processes.<sup>29</sup> The excited-state dynamics for these probe molecules have not been studied. Thus, it is worthwhile to further clarify the mechanism of fluorescent quenching for the probe molecules (HCM and HCH) and elaborate the relationship between fluorescent quantum yield and molecular structures.

In this work, we initially explained the TP fluorescence behavior of two experimental probes from a theoretical point, and analyzed the effect of substituent groups at different positions for OPA, TPA and fluorescence properties on the basis of two experimental probes. What's more, we designed some new hypochlorite-probing complexes and predicted their TPA properties. In addition, the vibronic coupling is also taken into account in the studies of fluorescence quantum yield and the mechanism of fluorescent quenching. We argue for the first time that the fluorescence quenching for the fluorescent probe containing the hydroxyl oxime is derived from the rapid internal conversion decay process. This study is hoped to provide useful theoretical guidelines for designing and synthesizing new TPA fluorescence probes with exceptional properties for detecting hypochlorite in mitochondria.

## 2. THEORETICAL METHODS

**2.1. Two-Photon Absorption.** A large two-photon absorption cross section  $\sigma^{\text{TPA}}$  is an important index for excellent fluorescent probes. The TPA cross section  $\sigma^{\text{TPA}}$  in GM units can be obtained from the two-photon transition probability  $\delta_{\text{au}}$  in atomic units using<sup>30,31</sup>

$$\sigma^{\text{TPA}} = \frac{4\pi^2 \alpha a_0^5 \omega^2}{15c\Gamma} \delta_{\text{au}} \quad (1)$$

where  $\alpha$  is the fine structure constant,  $a_0$  is the Bohr radius,  $\omega$  is the photon energy in atomic units,  $c$  is the speed of light, and  $\Gamma$  is the broadening factor which describes the spectral broadening of an excitation.  $\Gamma$  has been assumed to be 0.1 eV in order to make the theoretical simulation process consistent with the experimental spectra, measurement, and this value commonly has been used.<sup>32</sup> The transition probability  $\delta_{\text{au}}$  can be obtained from the TPA transition tensor  $S$  as<sup>33,34</sup>

$$\delta_{\text{au}} = \frac{1}{30} \sum_{ab} (FS_{aa}\bar{S}_{bb} + GS_{ab}\bar{S}_{ab} + HS_{ab}\bar{S}_{ba}) \quad (2)$$

Here,  $a, b \in \{x, y, z\}$  and the values  $F, H$ , and  $G$  are 2, 2, and 2 for linearly polarized light with parallel polarization and  $-2, 3$ , and 2 for the circular case. In the electric dipole approximation,

the TPA transition tensor  $S^{if}$  between the initial state  $i$  and the final state  $f$  is defined as<sup>31</sup>

$$S_{ab}^{if}(\omega_1, \omega_2) = \frac{1}{\hbar} \sum_{n \neq i} \left\{ \frac{\langle i|\mu_a|n\rangle \langle n|\mu_b|f\rangle}{\omega_{ni} - \omega_1} + \frac{\langle i|\mu_b|n\rangle \langle n|\mu_a|f\rangle}{\omega_{ni} - \omega_2} \right\} \quad (3)$$

where  $\langle i|\mu_a|n\rangle$  is the  $a$ th component of the transition dipole moment between the electronic states  $i$  and  $n$ .  $n$  is one of the possible intermediate states,  $\omega_{in}$  is associated excitation energy, and  $\omega_1$  and  $\omega_2$  are the energies of the two photons, respectively.

The TPA parameters such as the transition tensor  $S^{if}$ , two-photon transition probability  $\delta_{\text{au}}$ , and two-photon absorption cross section  $\sigma^{\text{TPA}}$  can be calculated with the help of quadratic response theory using the DALTON program.<sup>35</sup>

**2.2. The Fluorescence Quantum Yield.** The fluorescence quantum yield can be expressed as

$$\Phi = \frac{k_r}{k_r + k_{\text{nr}}} \quad (4)$$

Here,  $k_r$  is the radiative decay rate and  $k_{\text{nr}}$  is the nonradiative decay rate including the internal conversion rate and intersystem crossing rate.

The spontaneous emission rate ( $k_r$ ) is the integration of the emission spectrum:<sup>36</sup>

$$k_r = \int_0^\infty \sigma_{\text{em}}(\omega) d\omega \quad (5)$$

According to Fermi's golden rule,  $\sigma_{\text{em}}(\omega)$  is expressed as<sup>37</sup>

$$\sigma_{\text{em}}(\omega) = \frac{4\omega^3}{3c^3} \sum_{v_i, v_f} P_{v_i}(T) |\langle \Theta_{f v_f} | \vec{\mu}_f | \Theta_{i v_i} \rangle|^2 \times \delta(E_{if} + E_{v_i} - E_{v_f} - \hbar\omega) \quad (6)$$

where  $\sigma_{\text{em}}(\omega)$  is defined as the rate of spontaneous photon emission per unit frequency between  $\omega$  and  $\omega + d\omega$  per molecule.  $c$  is the velocity of light, and  $P_{v_i}(T)$  is the Boltzman distribution function for the initial vibronic state. The electric transition dipole moment is expressed as  $\vec{\mu}_f = \langle \Phi_f | \vec{\mu} | \Phi_i \rangle$ . Upon the Born–Oppenheimer approximation, the initial wave function  $|\Psi_{v_i}\rangle = |\Phi_i \Theta_{v_i}\rangle$  is described by the products of the electronic states  $|\Phi_i\rangle$  and the vibrational states  $|\Theta_{v_i}\rangle$ , which are the same as the final wave function.  $E_{if}$  is the difference of adiabatic energy between two states.  $E_{v_i}$  and  $E_{v_f}$  are the vibrational energies in the corresponding electronic states. According to the Franck–Condon approximation,  $\sigma_{\text{em}}(\omega)$  is defined as  $\sigma_{\text{em}}^{\text{FC}}(\omega)$ . The delta function is Fourier transformed as

$$\sigma_{\text{em}}^{\text{FC}}(\omega) = \frac{2\omega^3}{3\pi\hbar c^3} |\vec{\mu}_0|^2 \int_{-\infty}^{+\infty} e^{-i(\omega - \omega_f)t} Z_{v_i}^{-1} \rho_{\text{em},0}^{\text{FC}}(t, T) dt \quad (7)$$

Here,  $Z_{v_i}^{-1}$  is the partition function.  $\rho_{\text{em},0}^{\text{FC}}(t, T)$  is the thermal vibration correlation function, which is shown in the refs 36 and 38.

The internal conversion rate ( $k_{\text{ic}}$ ) is defined as<sup>39</sup>

$$k_{\text{ic}} = \frac{2\pi}{\hbar} |H'_{fi}|^2 \delta(E_{fi} + E_{v_f} - E_{v_i}) \quad (8)$$

and the non-Born–Oppenheimer coupling is expressed as<sup>40</sup>

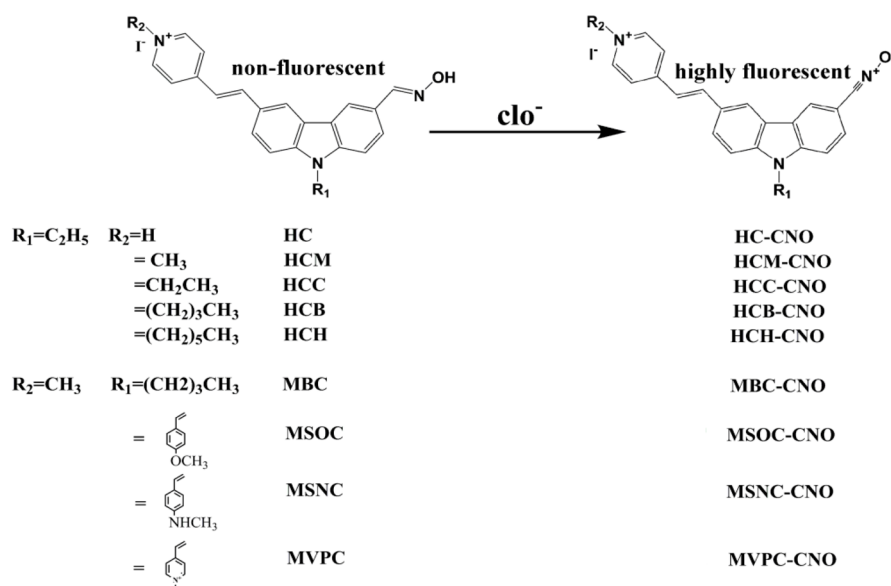


Figure 1. Structures and corresponding names of the investigated molecules.

$$H'_{fi} = -\hbar^2 \sum_l \left\langle \Phi_f | \Theta_{f\nu_f} \left| \frac{\partial \Phi_i}{\partial Q_{fl}} \frac{\partial \Theta_{i\nu_i}}{\partial Q_{fl}} \right. \right\rangle \quad (9)$$

Applying the Condon approximation, eq 9 is described as<sup>38</sup>

$$H'_{fi} = \sum_l \langle \Phi_f | \hat{P}_{fl} | \Phi_i \rangle \langle \Theta_{f\nu_f} | \hat{P}_{fl} | \Theta_{i\nu_i} \rangle \quad (10)$$

After insertion of eq 10 into eq 8 and the delta function being Fourier transformed, the IC rate can be expressed as<sup>36</sup>

$$k_{ic,kl} = \frac{1}{\hbar^2} R_{kl} \int_{-\infty}^{+\infty} e^{i\omega_{if}t} Z_{iv}^{-1} \rho_{ic,kl}(t, T) dt \quad (11)$$

Here,

$$R_{kl} = \langle \Phi_f | \hat{P}_{fk} | \Phi_i \rangle \langle \Phi_i | \hat{P}_{fl} | \Phi_f \rangle \quad (12)$$

The definition of  $Z_{iv}^{-1}$  and  $\rho_{ic,kl}(t, T)$  is similar to the description above. Both the radiative decay rate ( $k_r$ ) and the nonradiative decay rate ( $k_{nr}$ ) can be calculated using the MOMAP program.<sup>41</sup>

In this paper, we have optimized the ground-state and excited-state structures of all studied molecules at the B3LYP/6-31G(d,p) level of theory using the Gaussian 09 program package.<sup>42</sup> On the optimized geometries, we have carried out the frequency calculation, and no imaginary frequency has been found. After that, we have evaluated the electronic structure, one-photon absorption (OPA) and two-photon absorption (TPA) spectra at the CAM-B3LYP/6-31+G(d) level using the Gaussian 09 program.<sup>42</sup> Due to the obvious charge-transfer character of the studied molecules, we have used a range separated CAM-B3LYP functional.<sup>43–46</sup> At the same time, we also calculated molecular absorption spectral properties at the B3LYP/6-31+G(d) level of theory, which strongly underestimated the first excitation energy (see Table S1 in the Supporting Information). However, the results performed by Coulomb-attenuated CAM-B3LYP theory are in better agreement with the experimental values due to the improved long-range interactions. The TPA parameters were obtained by using quadratic response theory<sup>47</sup> in the same level, and the calculations were performed with the time-dependent density

functional theory (TD-DFT) as implemented in the DALTON program package.<sup>35</sup> The polarizable continuum model (PCM)<sup>48</sup> has been applied to consider the solvent effects. In addition, for all of the investigated compounds, the radiative rate and nonradiative decay rate constants are calculated using the MOMAP program<sup>41</sup> developed by Shuai et al., while the normal mode displacements and Duschinsky rotation matrix are calculated using the DUSHIN program.<sup>49,50</sup>

### 3. RESULTS AND DISCUSSION

#### 3.1. Molecular Design and Geometry Optimization.

The structures and names of the investigated molecules in this work are presented in Figure 1. A series of carbazole-based derivatives can be obtained by attaching different substituents at the R1 and R2 positions on the carbazole core.<sup>17,24,51</sup> The two-photon fluorescent properties of both probes HCM and HCH including reaction products (HCM-CNO and HCH-CNO) were experimentally measured.<sup>23</sup> Both of them possess large two-photon absorption cross sections ( $\delta_{TPA}$ ); nevertheless, the properties of HCH-CNO are better. To understand the influence of alkyl chains on molecular photophysical properties, molecules HC (HC-CNO), HCC (HCC-CNO), and HCB (HCB-CNO) have been designed by changing the length of alkyl chains at the R2 position, named the R2-series. Moreover, the neutral molecule HC-N (see Figure S1) is utilized to investigate the influence of cationic pyridinium moieties on optical properties. Furthermore, as we all know, different donors and acceptors have a great impact on the intramolecular charge transfer (ICT) properties, which affect OPA and TPA properties. In order to further explore the role of different electron-donating/withdrawing groups as substituents on OPA and TPA properties, MBC (MBC-CNO), MSOC (MSOC-CNO), MSNC (MSNC-CNO), and MVPC (MVPC-CNO) are obtained by introducing different electron-donors or electron-acceptors at the R1 position, named the R1-series.

In this work, molecular structures were optimized at the B3LYP/6-31G(d,p) level of theory by using the Gaussian 09 program.<sup>42</sup> The ground-state and the first excited-state structures are shown in Figure S1 in the Supporting Information. The results show the experimental molecules

(HCM, HCH, HCM-CNO, and HCH-CNO) have good planarity, and all atoms are in the same plane except for the alkyl chains at the R1 and R2 positions, which slightly affect the parent molecular geometry. In addition, geometry modifications between two states for the R2-series are not apparent. Conversely, the dihedral angles between the carbazole fragments and the substituents at the R1 position for the MSOC (MSOC-CNO) and MSNC (MSNC-CNO) are decreased from the ground state (at about  $40^\circ$ ) to the excited state (at about  $20^\circ$ ). For MVPC (MVPC-CNO), the 1-methyl-4-vinylpyridium group at the R1 position is twisted about  $20^\circ$  from the parent molecular plane at the ground state, while the dihedral angle is so large at the first excited state that the substituent is nearly perpendicular to the carbazole part.

### 3.2. Electronic Structure and One-Photon Absorption.

Electronic structure is important for fundamental understanding and interpretation of the absorption properties. To investigate the relationship between the geometric and electronic structures, the frontier molecular orbital energy levels as well as the energy gap  $\Delta E_{\text{H-L}}$  (the energy gap between the highest occupied molecular orbital (HOMO) and the lowest unoccupied molecular orbital (LUMO)) are calculated and described schematically in Figure 2. As shown in Figure 2,  $\Delta E_{\text{H-L}}$  ( $<3$  eV) for the cationic compound with an alkyl chain at the R2 position (see Figure 1) becomes smaller than that of the neutral molecule HC-N (3.702 eV). It should be pointed out that there is a slight gap change with the increase of the alkyl chains, which results in similar absorption and emission

spectra of these molecules (with alkyl chains at the R2 or R1 position). In addition, by modifying molecular structures at the R1 position with different electron-donating groups, such as 1-methoxy-4-vinylbenzene and 1-methylamino-4-vinylbenzene, respectively, the  $\Delta E_{\text{H-L}}$  values decrease dramatically, which is in the order HCM-CNO (2.915 eV)  $>$  MBC-CN (2.907 eV)  $>$  MSOC-CNO (2.585 eV)  $>$  MSNC-CNO (2.253 eV). It demonstrates that electron-donors at the R1 position are conducive to the decrease of  $\Delta E_{\text{H-L}}$  because the electron-donors can increase the energy of the HOMO obviously. In contrast to HCM-CNO, the energy gap  $\Delta E_{\text{H-L}}$  of MVPC-CNO (2.982 eV) increases, indicating the electron-acceptor (1-methyl-4-vinylpyridium) at the R1 position reduces effectively the HOMO level. Consequently, the alkyl groups at the R2 position have a primary influence on the LUMO energy values, giving rise to the decrease of  $\Delta E_{\text{H-L}}$ . However, the substituent groups at the R1 position mainly affect the energy of the HOMO. The electron-donors bring down  $\Delta E_{\text{H-L}}$ , while the electron-acceptors increase  $\Delta E_{\text{H-L}}$ , thus leading to a red-shift or blue-shift of the absorption and emission spectra, which is discussed below. Moreover, changing the length of the alkyl chain at the R1 or R2 position slightly affects the energy gap.

The OPA properties of the experimental compounds calculated by TD-DFT theory using different functionals are given in Table S1 in the Supporting Information. The OPA properties including the maximal OPA wavelengths ( $\lambda_{\text{max}}^0$ ), the corresponding oscillator strengths ( $f$ ), the transition moment, the transition nature, and weights for all of the investigated compounds calculated at the CAM-B3LYP/6-31+G(d) level of theory in water solvent are listed in Table S2 in the Supporting Information. It can be seen that the calculated maximum absorption peaks of HCM, HCM-CNO, HCH, and HCH-CNO (414, 407, 412, and 405 nm, respectively) are in good agreement with the experimental data<sup>23</sup> (419, 413, 422, and 416 nm, respectively). In addition, the relevant one-photon absorption spectra are obtained by using Lorentzian broadening, as illustrated in Figure 3. The spectral shapes are consistent with the experimental results. As clearly shown in Table S2 and Figure 3, there are three main absorption peaks (407/414, 255/260, and 233/242 nm) in HCM-CNO/HCM and a shoulder peak at 298/292 nm. For the maximum absorption peak of HCM-CNO, the major contribution in the  $S_0 \rightarrow S_1$  transition comes from HOMO  $\rightarrow$  LUMO, and the transition has more  $\pi-\pi^*$  character. Besides, the other molecules have similar character. However, the transition natures of the other absorption peaks are more complicated, and the detailed analysis by hole-electron distribution is listed in Figure S3. It should be pointed out that the maximum absorption peaks for cationic compounds (about 410 nm) are red-shifted compared with those of the neutral molecule HC-N (332 nm), because the energy level of the LUMO goes downward and the  $\Delta E_{\text{H-L}}$  decreases, as shown in the analysis above. Moreover, the effect on the OPA absorption wavelength is slight by changing the length of the alkyl chains at the R1 or R2 position, which corresponds to their similar electronic structures.

In addition, we further assess the influence of substituents at the R1 position for OPA properties. Comparing with HCM-CNO (HCM), strong electron-donors have significant contributions for OPA, such as MSOC-CNO (MSOC) and MSNC-CNO (MSNC), which possess red-shifted maximum absorption wavelengths and enhanced oscillator strengths. The reason for this phenomenon is that the electron-donor

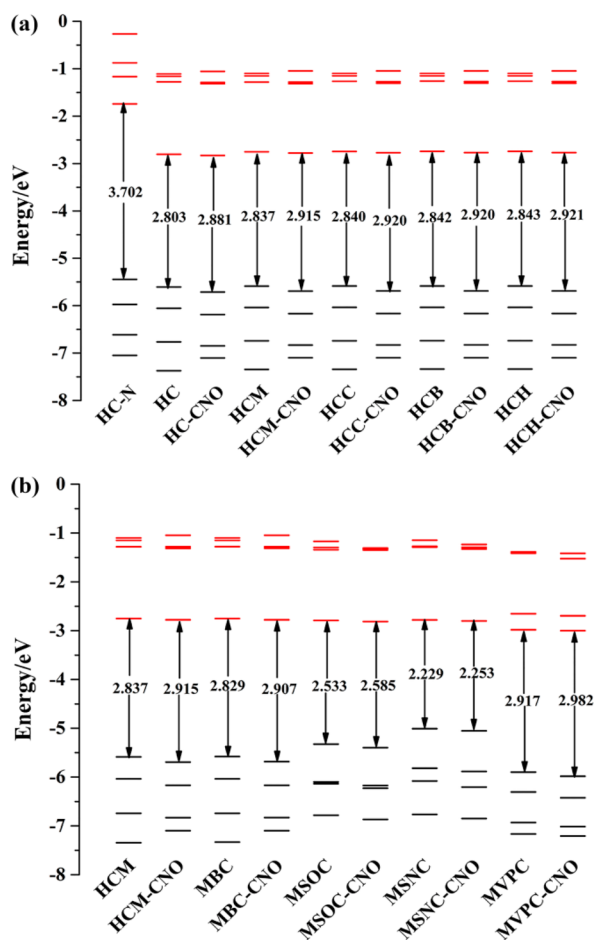


Figure 2. Calculated frontier molecular orbital energy levels.



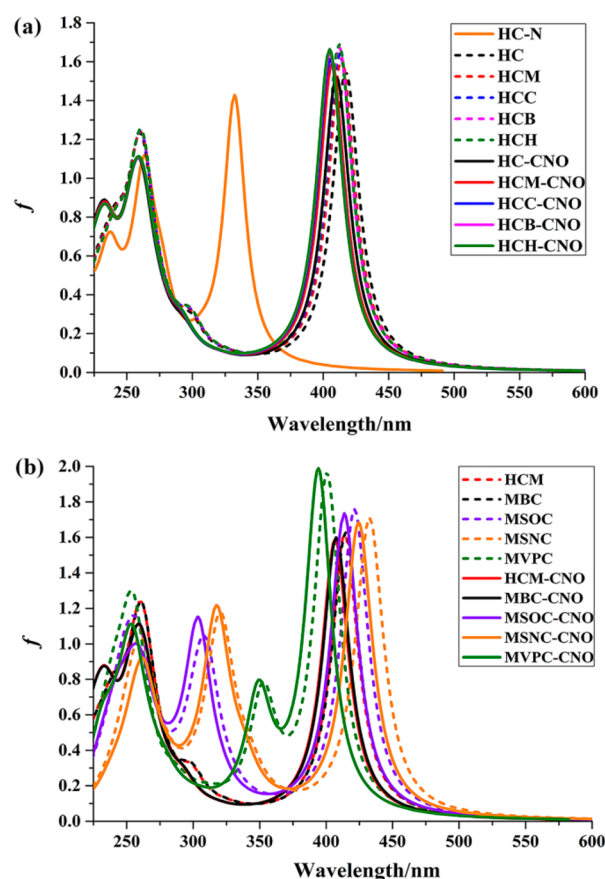


Figure 3. One-photon absorption spectra for the studied molecules.

decreases the energy gap and enhances charge transfer (CT) from the substituent at the R1 position to the pyridine moiety, as shown in Figure S2. Besides, there is another absorption peak at 304 nm for MSOC-CNO (339 nm for MSNC-CNO), which is the connection with the charge transfer between the carbazole and the substituent at the R1 position, which does not appear at HCM-CNO. On the contrary, the maximum absorption peak of MVPC-CNO (MVPC) is a hypsochromic shift, and the oscillator strength of MVPC-CNO (MVPC) is enhanced dramatically. For MVPC-CNO (MVPC), the maximum absorption peak at 394 nm (401 nm) comes from the electronic excitation of  $S_0 \rightarrow S_1$ , which can be assigned to the configuration HOMO  $\rightarrow$  LUMO (cf. Table S2). As shown in Figure S2, the charge on both the HOMO and the LUMO is distributed in the substituent 1-methyl-4-vinylpyridium group and the parent carbazole group, which is conducive to intramolecular charge transfer. By the way, there is a weak OPA peak at 352 nm (349 nm) for MVPC-CNO (MVPC) coming from the electronic excitation of  $S_0 \rightarrow S_2$ , and the corresponding transition character is governed by local excitation-charge transfer (LE-CT) mixing.

**3.3. The Excited-State, Fluorescence Property, and Fluorescence Off-On Effect.** The geometry optimization in the first excited state was obtained by the B3LYP functional with the 6-31G(d,p) basis set in water solvent. The emission spectra were calculated. The fluorescent emission wavelength is 543 nm (541 nm) for HCM-CNO (HCH-CNO), which is in good agreement with the experimental value of 544 nm for HCM-CNO (546 nm for HCH-CNO) in PBS buffer.<sup>23</sup> The fluorescence properties such as the emission wavelength ( $\lambda_{\text{ems}}$ ),

oscillator strength ( $f$ ), fluorescent lifetime ( $\tau$ ), and transition nature are given in Table S5. The fluorescent spectra of reaction products are shown in Figure 4. As shown in Table S5

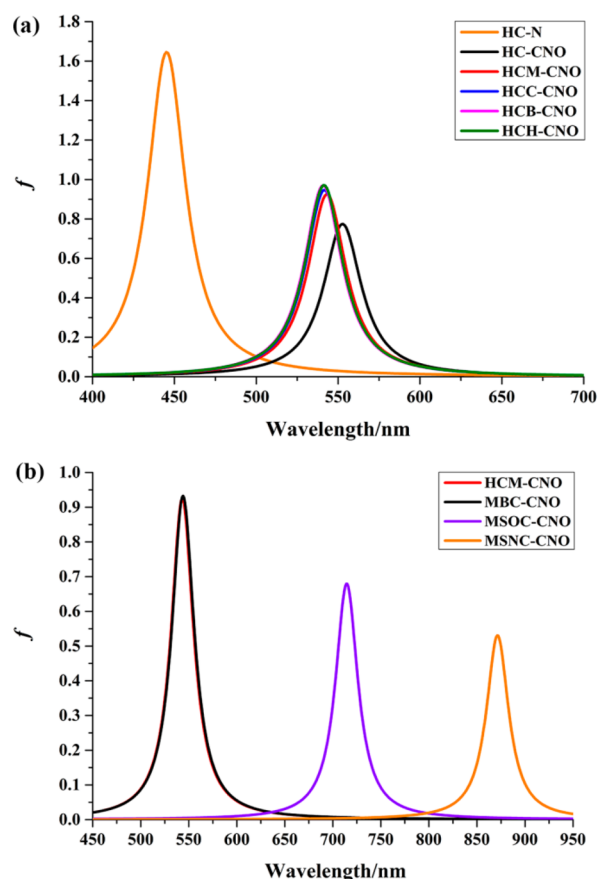


Figure 4. Fluorescence spectra for the studied molecules.

and Figure 4,  $\lambda_{\text{ems}}$  values of all of the studied molecules are derived from the radiative decay of  $S_1 \rightarrow S_0$  dominated by the transition from the HOMO to the LUMO. The effect of the alkyl chain on the fluorescent wavelength is not obvious, but it has a significant influence on the fluorescence quantum yield (discussed later). Compared with the neutral compound HC-N, the fluorescent emission spectra for cationic compounds are red-shifted and the oscillator strengths decrease. For compounds MSOC-CNO and MSNC-CNO, their  $\lambda_{\text{ems}}$  peaks appear around 714 and 871 nm in the near-infrared region. However, MVPC-CNO is fluorescence quenched due to the marked twisting of the 1-methyl-4-vinylpyridium moiety relative to the carbazole plane at the first excited state (see Figure S1); thus, the compound with a strong electron-acceptor at the R1 position is not suitable to be a fluorescent probe.

Furthermore, the fluorescence quantum yield ( $\Phi$ ) is a key index for the efficiency of probes. For probe molecules HCM and HCH, only weak fluorescence was observed in the experimental process, while the fluorescence is enhanced after reaction with hypochlorite. Previous reports consider that C=N isomerization is the predominant decay process of the excited states leading to fluorescence quenching.<sup>26–28</sup> However, our optimization results suggest that there is no obvious change for probe molecule structures in the excited state (see Figure S1) and no potential energy surfaces crossing. We speculate the nonradiation decay process may play a key role in the

**Table 1.** Fluorescence Properties Including the Vertical Excitation Energies ( $E_{\text{vt}}$ ), the Adiabatic Energy Difference between  $S_1$  and  $S_0$  ( $E_{\text{ad}}$ ), the Electric Transition Dipole Moments ( $\mu$ ), the Radiative Rates ( $k_{\text{r}}$ ), the Internal Conversion Rates ( $k_{\text{nr}}$ ), and the Corresponding Fluorescence Quantum Yield ( $\Phi$ ) Calculated by the B3LYP/6-31G (d,p) Method in Water Solvent<sup>a</sup>

molecules	$E_{\text{vt}}$ (eV)	$E_{\text{ad}}$ (eV)	$\mu$ (D)	$k_{\text{r}}$ ( $\text{s}^{-1}$ )	$k_{\text{nr}}$ ( $\text{s}^{-1}$ )	$\Phi$
HCM	2.09	2.29	8.73	$0.16 \times 10^8$	$1.51 \times 10^{11}$	0
HCH	2.10	2.30	8.89	$0.88 \times 10^8$	$4.62 \times 10^9$	0.019 (0.011)
HC–N	2.78	2.99	12.47	$5.07 \times 10^8$	$8.06 \times 10^4$	1.000
HC–CNO	2.24	2.38	9.53	$1.27 \times 10^8$	$9.93 \times 10^8$	0.114
HCM–CNO	2.28	2.40	10.33	$0.22 \times 10^8$	$1.05 \times 10^9$	0.020
HCC–CNO	2.29	2.41	10.43	$1.66 \times 10^8$	$3.83 \times 10^8$	0.302
HCB–CNO	2.29	2.41	10.56	$1.80 \times 10^8$	$1.91 \times 10^8$	0.485
HCH–CNO	2.29	2.41	10.56	$1.63 \times 10^8$	$1.10 \times 10^9$	0.129 (0.140)

<sup>a</sup>The values in parentheses are the experimental results.

deactivation of the excited state. Therefore, we calculated the radiative and nonradiative decay rates from  $S_1$  to  $S_0$  for R2-series compounds as well as fluorescent quantum yields, and obtained the relationship between structure and fluorescent quantum yield, as shown in Table 1 and Figure 5. We mainly

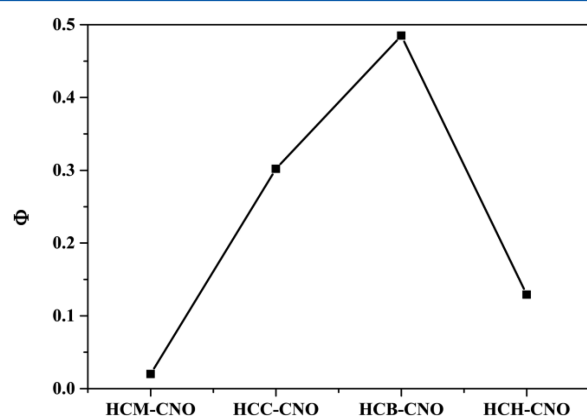


**Figure 5.** Relationship between fluorescence quantum yield and molecular structure.

analyzed the radiative decay rates and the internal conversion decay rates, because the intersystem crossing process can not compete with the two above (see Table S6 and Table 1; the rate of the intersystem crossing  $k_{\text{isc}}$  ( $\sim 10^6 \text{ s}^{-1}$ ) is much less than  $k_{\text{r}}$  ( $\sim 10^8 \text{ s}^{-1}$ )). As given in Table 1, the calculated fluorescent quantum yields are 0.019 and 0.129, which are in good agreement with the experimental values<sup>23</sup> of 0.011 and 0.140 for the probe HCH and corresponding reaction product HCH–CNO, respectively. What is interesting is that the fluorescent quantum yield is not proportional to the length of the alkyl chain. The HCB–CNO with butyl at the R2 position, rather than HCH–CNO with hexyl, possesses the largest quantum yield (0.485). The fluorescence enhancement after addition of  $\text{ClO}^-$  is due to the increased radiative rate and the decreased nonradiative rate. It can be seen that the values of vertical excitation energy and electric transition dipole moment for HCH–CNO (2.29 eV and 10.56 D) are larger than those for HCH (2.10 eV and 8.89 D), which contributes to increasing  $k_{\text{r}}$  rate. The nonradiative decay process is relatively complicated. From the IC rate formula (eq 11), the internal conversion decay rate is in connection with the electronic coupling and nuclear motion. The large adiabatic energy difference is adverse to the internal conversion process, while the large geometry change between the two states is in favor of the nonradiative transition.

The Huang–Rhys (HR) factor characterizes the amount of absorbed photons converted into phonons when transitioning from one electronic state to another and can also be used to quantify the geometry relaxation between two electronic states, which is important in determining the internal conversion rate.<sup>52</sup> The HR factors are calculated and depicted in Figure 6 for the investigated compounds. The following is clearly seen: (1) The modes with a nonzero HR factor mainly appear at the low frequency regime ( $< 500 \text{ cm}^{-1}$ ) for all cationic molecules. (2) The HR factor for the probe HCH (with a maximum value of 1.12) is much larger than that for the reaction product HCH–CNO (with a maximum value of 0.54). Such features indicate HCH may possess the Duschinsky rotation effect (DRE), which contributes to nonradiative transition  $S_1 \rightarrow S_0$ . (3) Nitrile oxide bends at  $501 \text{ cm}^{-1}$  and side-chain bends at  $30 \text{ cm}^{-1}$  possess large HR factors ( $> 1$ ) for HCM–CNO, leading to the larger IC rate and smaller fluorescence quantum yield than those for HCH–CNO. (4) The length of the alkyl groups has an important influence on the quantum yield (see Figure 5), though it hardly affects the emission wavelength. The molecule HCB–CNO possesses the largest quantum yield (0.485), because the huge electric transition dipole moment contributes to the radiative decay rate and the small HR factor leads to a decrease in the IC rate. (5) Compared to the cationic compounds, the extent of geometry relaxation is absolutely smaller for the neutral molecule, so that the radiative decay rate is found to be dominant for HC–N compound.

To further elucidate the structure–property relationship, the molecular geometry relaxation in the decay process of  $S_1 \rightarrow S_0$  needs to be estimated. Reorganization energy is a useful measure for the extent of geometry relaxation, which indicates the nonradiative channel for the excited-state decay. The reorganization energies and corresponding vibrational frequencies are given in Figure 7 and Figure S4. For the sake of clarity, we decomposed the organization energy into the internal coordinate relaxation shown in Figure 8 and Tables S7–S10. As shown in Figure 7 and Figure S4, it is clearly seen that the normal modes with large reorganization energies mainly appear at the high frequency region ( $> 1000 \text{ cm}^{-1}$ ) for reaction products except HCM–CNO. There is a high frequency mode (around  $1650 \text{ cm}^{-1}$ ) with the large reorganization energy ( $> 150 \text{ cm}^{-1}$ ) coming from skeletal stretches in all compounds. The reorganization energies for probes (HCM and HCH with values over  $250 \text{ cm}^{-1}$ ) are much larger than those for reaction products (HCM–CNO and HCH–CNO with values of about  $150 \text{ cm}^{-1}$ ), because of the larger geometry change for probes, as shown in Figure 8. It can be seen that the C1–N5 and C4–N5 bond length changes in the skeletal stretching mode (around

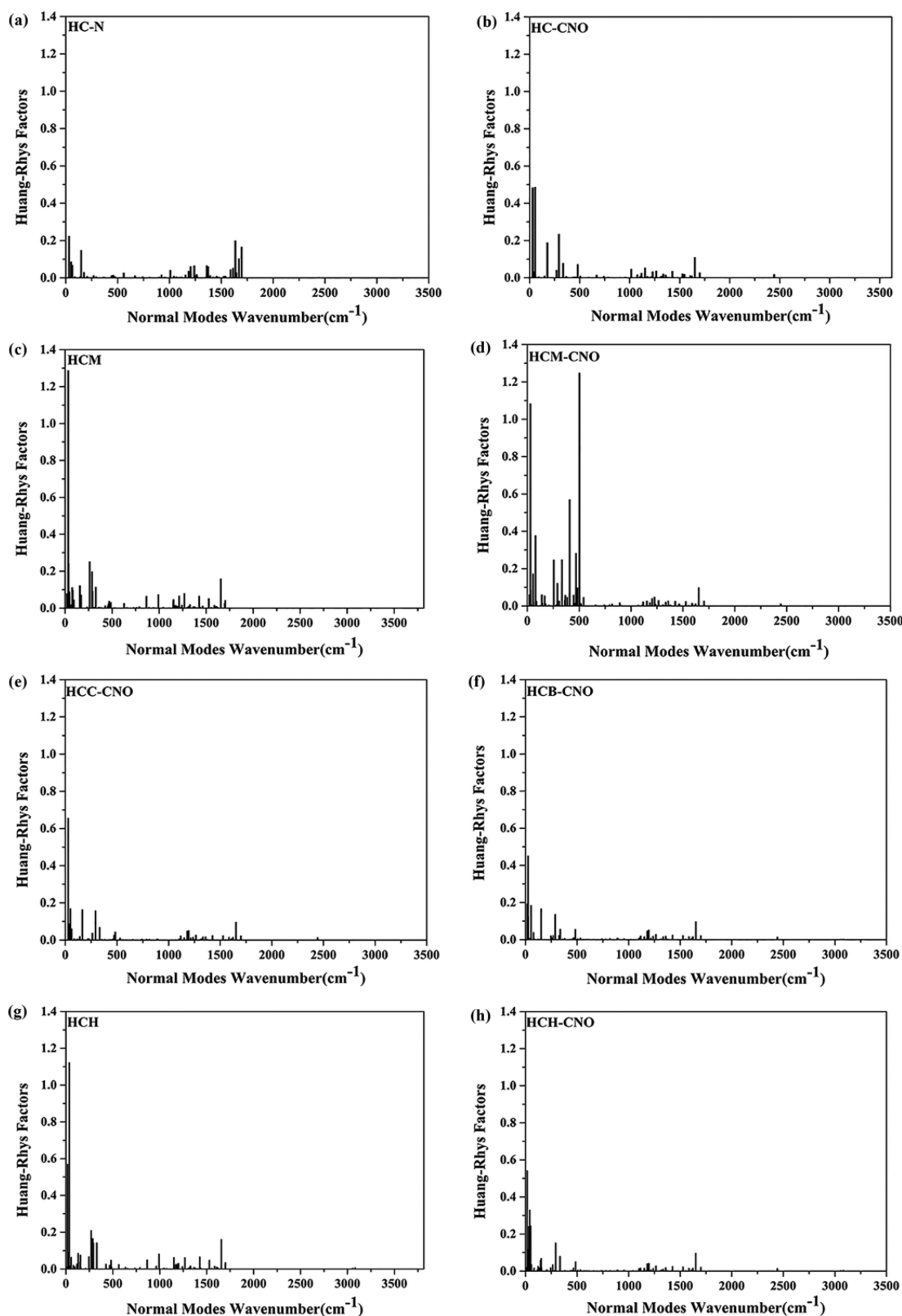
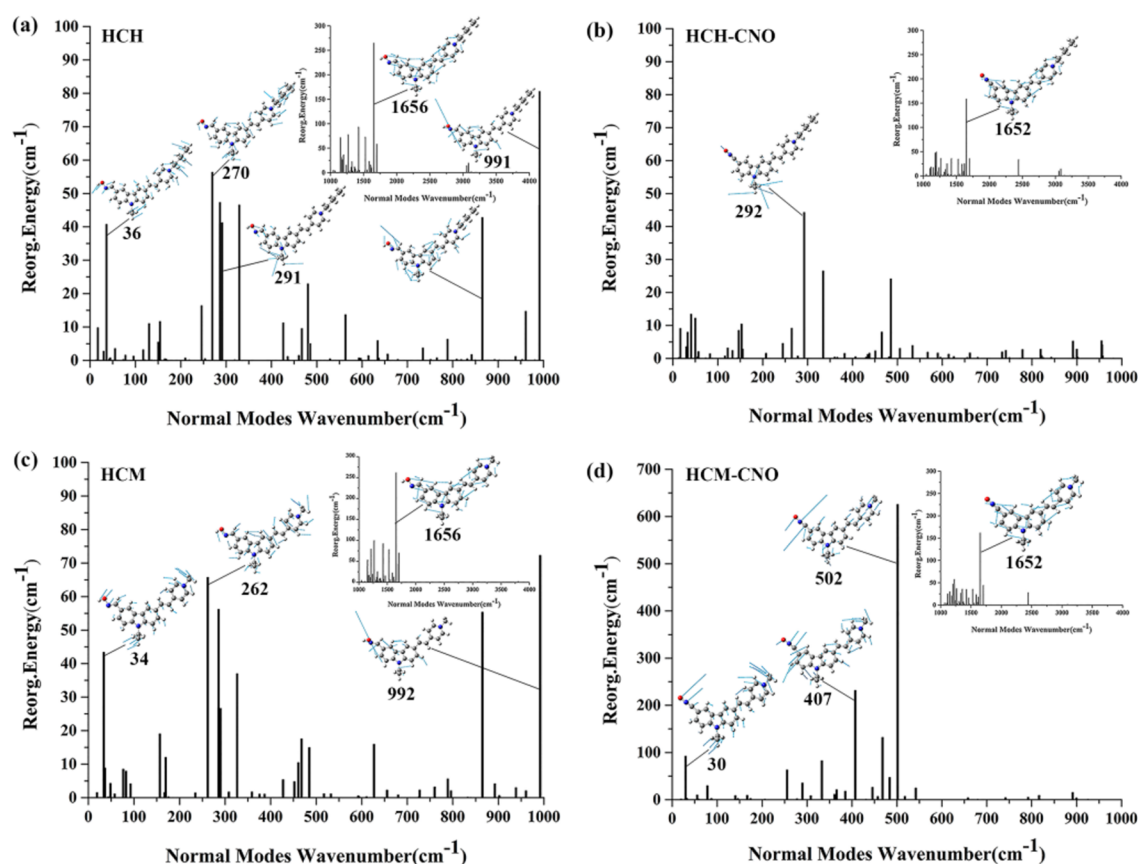


Figure 6. Huang–Rhys factors in terms of  $S_0$  surface.

1650  $\text{cm}^{-1}$ ) are larger for probes than those for reaction products. However, the key factor determining the difference of nonradiative rates for compounds is the contribution of the lower frequency ( $<1000 \text{ cm}^{-1}$ ) modes. The contribution of the low frequency ( $<1000 \text{ cm}^{-1}$ ) modes to the total reorganization

energy is more than 30% in probes HCH and HCM and about 25% in reaction product HCH–CNO, while it is 68% in HCM–CNO. Combining with displacement vectors in Figure 7, there is only one N–O bond stretching mode (991 or 992  $\text{cm}^{-1}$ ) with a large reorganization energy in both probes, 81



**Figure 7.** Calculated reorganization energies and the displacement vectors for the normal modes with large reorganization energies for experimental molecules (HCM, HCM-CNO, HCH, and HCH-CNO).

$\text{cm}^{-1}$  for HCH and  $72 \text{ cm}^{-1}$  for HCM. Moreover, the reorganization energies for probes which come from side-chain bending modes ( $<300 \text{ cm}^{-1}$ ) are much larger than those for reaction products. We can conclude that the stretching modes of oxime and the low-frequency motions of the side-chains are hindered after addition of  $\text{ClO}^-$ , and thus, their contributions to the internal conversion decay rate are strongly suppressed, leading to the quantum yield being increased and the fluorescence being enhanced. In addition, the largest reorganization energy ( $625 \text{ cm}^{-1}$ ) of HCM-CNO comes from the deformation of nitrile oxide ( $502 \text{ cm}^{-1}$ ), whose dihedral angle  $D(\text{C13}-\text{C12}-\text{O25}-\text{N24})$  and  $D(\text{C11}-\text{C12}-\text{O25}-\text{N24})$  changes are about  $13^\circ$  from  $S_1 \rightarrow S_0$ , resulting in the IC rate of HCM-CNO being larger than that of HCH-CNO. What's more, the neutral compound HC-N is also taken into account in studies of the structure-property relationship. The change of vibration quanta at the low-frequency region is obviously small for HC-N in sharp contrast to the cationic compounds, which contributes to suppressing the IC rate ( $10^4/\text{s}$ ).

Therefore, we can conclude that the increased quantum yield after addition of  $\text{ClO}^-$  results from the enhancement of the electric transition dipole moment and the adiabatic energy between two states and the suppression of both of C-N bond stretching and the side-chain bending motions in the low frequency region. The results show that the length of the alkyl chain has imposed a significant impact on vibronic coupling, and the compound HCB-CNO with butyl at the R2 position possesses the largest quantum yield (0.485) in all of the investigated compounds. The cationic pyridinium moiety not

only is the mitochondria-targeted functional group, but it also plays an important role in geometry relaxation, changing the optical properties of compounds.

**3.4. Two-Photon Absorption (TPA) Property.** **3.4.1. The Calculations of TPA Properties.** As stated earlier, the main purpose of the present study is aimed at investigating the relationship between the TPA properties and structures. In order to evaluate the two-photon response for the investigated molecules, we calculated and analyzed TPA properties including the maximum TPA cross sections ( $\sigma_{\text{max}}^{\text{TPA}}$ ) and corresponding TPA wavelengths ( $\lambda_{\text{max}}^{\text{TPA}}$ ) in the NIR spectral region with the help of quadratic response theory at the CAM-B3LYP/6-31+G(d) level. The results are listed in Table 2. The calculated  $\sigma_{\text{max}}^{\text{TPA}}$  values of HCM, HCM-CNO, HCH, and HCH-CNO are 457, 434, 501, and 475 GM at 824, 810, 821, and 808 nm, respectively. It is interesting to note that the TPA cross section of HCH-CNO (HCM-CNO) can reach up to 5990 GM (5510 GM) at 509 nm, which is corresponding to the OPA at about 255 nm. However, this excited wavelength is not suitable for biological fields. They may have a great research value in optical limiting. As shown in Table 2, the calculated  $\lambda_{\text{max}}^{\text{TPA}}$  values in the NIR spectral region are in good agreement with the experimental results,<sup>23</sup> while the calculated  $\sigma_{\text{max}}^{\text{TPA}}$  values are smaller than the experimental values, but the variation tendency is coincident. In order to further ensure the accuracy of the calculation method, we also performed the calculations on  $\lambda_{\text{max}}^{\text{TPA}}$  and  $\sigma_{\text{max}}^{\text{TPA}}$  of MBC\* (in MeCN solvent) at the same calculated level, which agreed well with the experimental results.<sup>17</sup> It is no doubt that the results can provide the correct



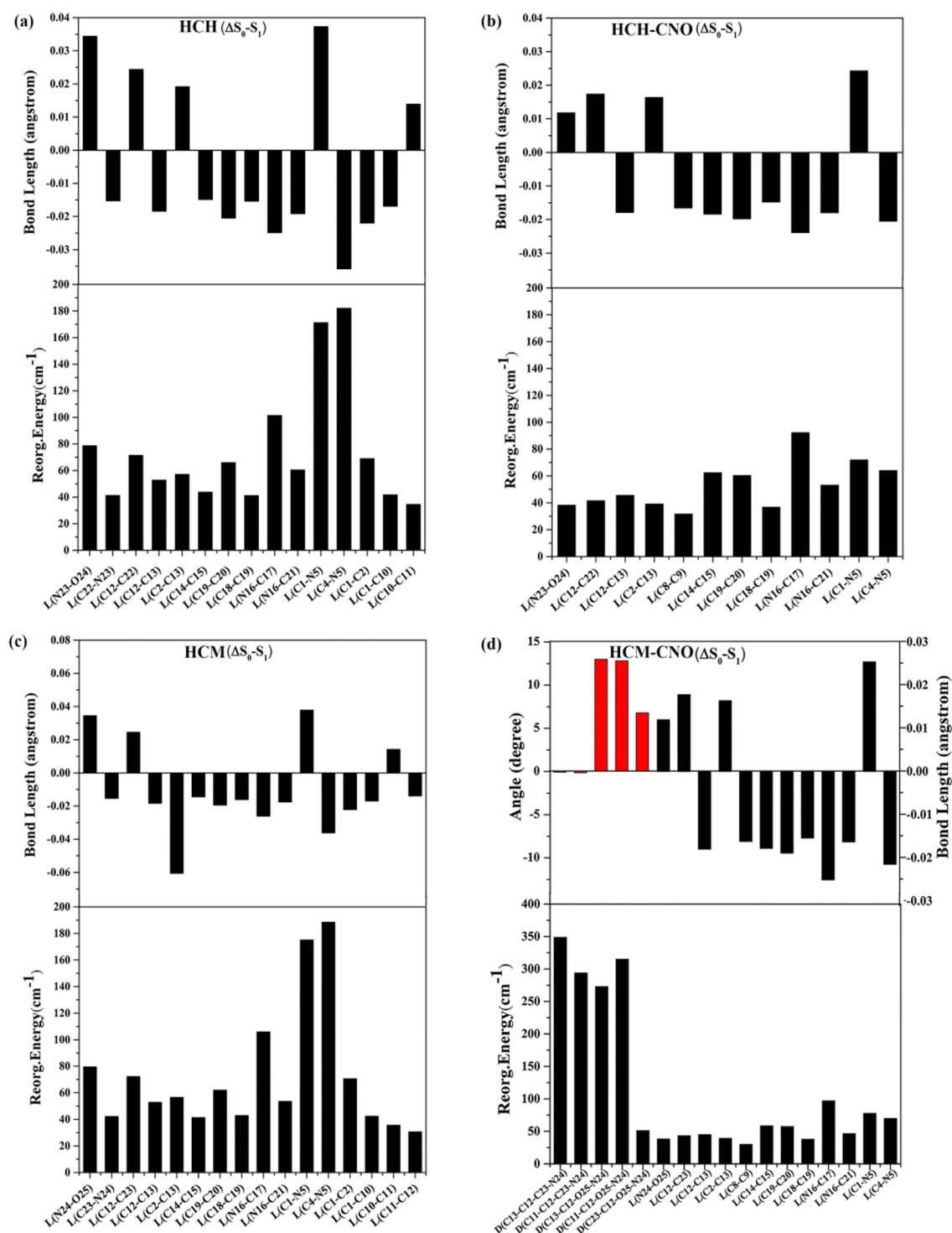


**Figure 8.** Large reorganization energies (>30 cm<sup>-1</sup>, bottom) and corresponding coordinate modifications between S<sub>0</sub> and S<sub>1</sub> (top, the black columns are for lengths and the red columns are for dihedral angles).

relationship between the structures and the TPA properties for the investigated molecules.

**3.4.2. The Structural Aspects of TPA Properties.** As mentioned above, the molecules are designed by introducing different lengths of alkyl chains at the R2 or R1 position, as well as electron-donors and electron-acceptors at the R1 position of the carbazole core. As shown in Figure 9, the maximum TPA cross section becomes larger as the alkyl chain becomes longer. It is worth mentioning that the  $\sigma_{\max}^{\text{TPA}}$  is not proportional to the

length of the chain, and the influence of the alkyl chain on  $\lambda_{\max}^T$  is slight, which is the same as the case of OPA. Interestingly, the maximum TPA cross section for the neutral compound HC-N (144 GM) is much smaller than that for the cationic compounds (e.g., 387 GM for HC-CNO). Besides, the corresponding TPA spectrum of HC-CNO (816 nm) is red-shifted to the NIR region compared with HC-N (667 nm).

Moreover, the effect of strong electron-donating or -accepting groups is more significant for the magnitude of TPA cross

Table 2. TPA Properties of the Molecules Calculated Using Quadratic Response Theory

molecules	$\lambda_{\max}^T$ <sup>a</sup> (nm)	$\sigma_{\max}^{\text{TPA}}$ <sup>a</sup> (GM)	$\lambda_{\max}^T$ <sup>b</sup> (nm)	$\sigma_{\max}^{\text{TPA}}$ <sup>b</sup> (GM)	transition nature <sup>b</sup>		
HC–N			666.59	144	$S_0 \rightarrow S_1$	H $\rightarrow$ L	86.00%
HC			829.33	405	$S_0 \rightarrow S_1$	H $\rightarrow$ L	85.95%
HC–CNO			815.69	387	$S_0 \rightarrow S_1$	H $\rightarrow$ L	86.70%
HCM			823.82	457	$S_0 \rightarrow S_1$	H $\rightarrow$ L	85.68%
			522.04	4670	$S_0 \rightarrow S_6$	H–2 $\rightarrow$ L	47.10%
HCM–CNO	860	980.0				H $\rightarrow$ L+1	15.00%
			810.36	434	$S_0 \rightarrow S_1$	H $\rightarrow$ L	86.45%
			509.18	5510	$S_0 \rightarrow S_7$	H–2 $\rightarrow$ L	40.63%
						H $\rightarrow$ L+3	33.27%
HCC			821.09	478	$S_0 \rightarrow S_1$	H $\rightarrow$ L	85.43%
HCC–CNO			807.72	454	$S_0 \rightarrow S_1$	H $\rightarrow$ L	86.22%
HCB			822.42	493	$S_0 \rightarrow S_1$	H $\rightarrow$ L	85.25%
HCB–CNO			807.72	467	$S_0 \rightarrow S_1$	H $\rightarrow$ L	86.05%
HCH			821.09	501	$S_0 \rightarrow S_1$	H $\rightarrow$ L	85.21%
			522.04	5190	$S_0 \rightarrow S_6$	H–2 $\rightarrow$ L	45.89%
HCH–CNO	860	1642.2				H $\rightarrow$ L+1	15.36%
			807.72	475	$S_0 \rightarrow S_1$	H $\rightarrow$ L	86.01%
			509.18	5990	$S_0 \rightarrow S_7$	H–2 $\rightarrow$ L	42.63%
MBC						H $\rightarrow$ L+2	24.07%
			823.83	468	$S_0 \rightarrow S_1$	H $\rightarrow$ L	85.70%
			810.36	444	$S_0 \rightarrow S_1$	H $\rightarrow$ L	86.45%
MBC* <sup>c</sup>	810	522	797.33	530	$S_0 \rightarrow S_1$	H $\rightarrow$ L	87.94%
MSOC			837.74	730	$S_0 \rightarrow S_1$	H $\rightarrow$ L	71.78%
MSOC–CNO						H–1 $\rightarrow$ L	19.34%
			823.82	677	$S_0 \rightarrow S_1$	H $\rightarrow$ L	69.68%
						H–1 $\rightarrow$ L	22.42%
MSNC			858.03	970	$S_0 \rightarrow S_1$	H $\rightarrow$ L	57.00%
			679.37	862	$S_0 \rightarrow S_2$	H–1 $\rightarrow$ L	31.78%
						H $\rightarrow$ L	27.66%
						H–2 $\rightarrow$ L	26.95%
MSNC–CNO			843.44	906	$S_0 \rightarrow S_1$	H $\rightarrow$ L	52.71%
						H–1 $\rightarrow$ L	36.89%
			672.01	822	$S_0 \rightarrow S_2$	H–1 $\rightarrow$ L	35.03%
						H $\rightarrow$ L	33.89%
MVPC						H–2 $\rightarrow$ L	18.48%
			797.33	133	$S_0 \rightarrow S_1$	H $\rightarrow$ L	76.72%
			702.46	1020	$S_0 \rightarrow S_2$	H $\rightarrow$ L+1	66.51%
MVPC–CNO						H–1 $\rightarrow$ L	16.47%
			744.65	204	$S_0 \rightarrow S_1$	H $\rightarrow$ L	78.55%
			686.90	1070	$S_0 \rightarrow S_2$	H $\rightarrow$ L+1	69.80%
						H–1 $\rightarrow$ L	13.85%

<sup>a</sup>Experimental data. <sup>b</sup>The results were computed at the CAM-B3LYP/6-31+G(d) level of theory using DALTON programs in water solvent.

<sup>c</sup>MBC\* was computed at the CAM-B3LYP/6-31+G(d) level of theory using DALTON programs in MeCN solvent.

section. The designed compounds MSOC–CNO (MSOC), MSNC–CNO (MSNC), and MVPC–CNO (MVPC) possess excellent TPA properties. The calculated results from Table 2 and Figure 9 demonstrate that the MSOC–CNO (MSOC) and MSNC–CNO (MSNC) bearing the 1-methoxy-4-vinylbenzene and 1-methylamino-4-vinylbenzene respectively exhibit better TPA properties than those of molecules with alkyl groups. They possess larger TPA cross sections and red-shifted spectra, MSNC–CNO (906 GM, 843 nm) > MSOC–CNO (677 GM, 824 nm) > HCM–CNO (434 GM, 810 nm), attributing to the strong electron-donors that are conducive to improving intramolecular charge transfer and decreasing the  $\Delta E_{\text{H-L}}$ . The TPA transitions of MSOC–CNO (MSOC) and MSNC–CNO (MSNC) come from the electronic excitation of  $S_0 \rightarrow S_1$ , the configuration HOMO  $\rightarrow$  LUMO weights ca. 50–80% and

HOMO–1  $\rightarrow$  LUMO weights ca. 20–37%. As shown in contour surfaces of the frontier molecular orbitals (see Figure S2), the electron transfers from 1-methoxy-4-vinylbenzene or 1-methylamino-4-vinylbenzene to electron-acceptor, which enhances charge transfer moment, contributing to the increase of transition moment and TPA cross section. The large TPA cross sections in the NIR region indicate that the two chromophores can be regarded as suitable candidates for two-photon fluorescent probes. In addition, the other large TPA cross section of MSNC–CNO is 822 GM at 672 nm, which comes from the electronic excitation of  $S_0 \rightarrow S_2$  with CT character. The similar phenomenon is also observed for probe MSNC. As for MVPC–CNO, the  $\sigma_{\max}^{\text{TPA}}$  (1070 GM) is formed with the electronic excitation of  $S_0 \rightarrow S_2$  at 687 nm rather than the excitation from the ground state to the first excited singlet state.

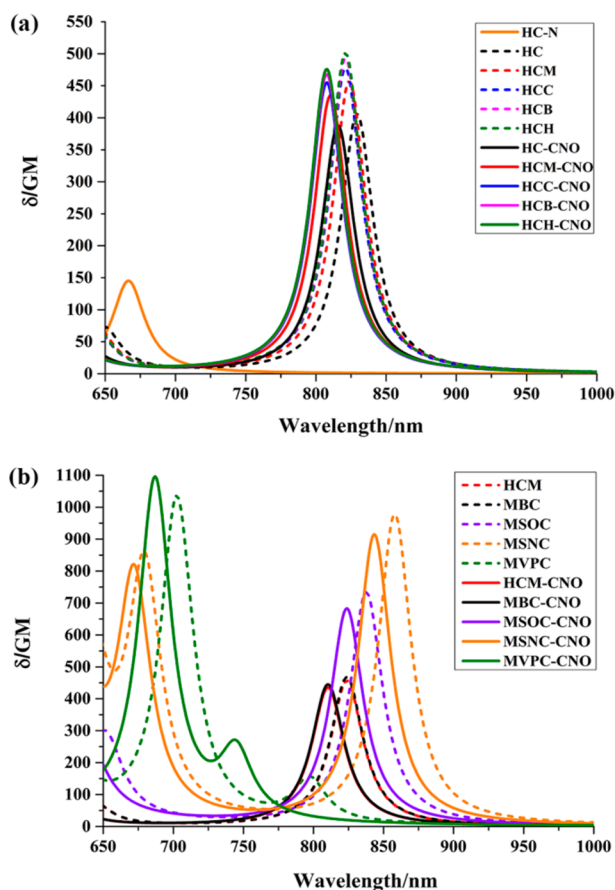


Figure 9. Two-photon absorption spectra for the studied molecules.

By the analysis of hole–electron distribution, the transition character of MVPC–CNO is governed by LE–CT mixing over the entire molecule, which can be described as a mixture of configurations  $\text{HOMO} \rightarrow \text{LUMO}+1$  and  $\text{HOMO}-1 \rightarrow \text{LUMO}$ .

**3.4.3. The TPA Tensor Elements ( $S_{ab}$ ) and TPA Cross Section.** In order to further explain the TPA properties originate from which specific molecular moieties of investigated molecules, the TPA tensor elements ( $S_{ab}$ ) are calculated and analyzed with the help of quadratic response theory at the CAM-B3LYP/6-31+G(d) level. The relationship between TPA cross section ( $\sigma^{\text{TPA}}$ ) in GM units and the TPA tensor elements ( $S_{ab}$ ) is given by formulas 1 and 2 in section 2. For a two-photon excitation by a linearly polarized single beam of light,  $\delta_{\text{au}}$  in atomic units is evaluated by the expression<sup>53,54</sup>

$$\delta_{\text{au}} = 6(S_{xx}^2 + S_{yy}^2 + S_{zz}^2) + 8(S_{xy}^2 + S_{xz}^2 + S_{yz}^2) + 4(S_{xx}S_{yy} + S_{yy}S_{zz} + S_{xx}S_{zz}) \quad (13)$$

The TPA tensor elements  $S_{ab}$  and the TPA cross sections  $\delta_{\text{au}}$  (in au) for the relevant excited states of the studied molecules are shown in Table 3. The results clearly show that the TPA tensor element  $S_{xx}$  component has a major contribution to the two-photon absorption process for the studied excited states of all molecules. The  $S_{xy}$ ,  $S_{yy}$ , and  $S_{xz}$  components have some moderate contributions, but the rest of the TPA tensor elements ( $S_{yz}$  and  $S_{zz}$ ) barely affect the  $\delta_{\text{au}}$  values, because of the good planar rigidity of the parent molecular frame. Contributions of  $S_{xx}$  and  $S_{xz}$  are more remarkable as the length of alkyl chains increasing at the R2 and R1 positions, leading to

the TPA cross section increasing. It is clear that the increased  $\delta_{\text{au}}$  value is largely concerned with the electronic transition in the  $x$  direction shown in Figure S2. Moreover, the values of  $S_{xx}$  and  $S_{xy}$  for cationic compound HC–CNO (512.1 and 120.5) are around twice as large as those for neutral compound HC–N (257.2 and 66.0).

Similarly, contributions of  $S_{xx}$  and  $S_{xy}$  are improved remarkably by introducing strong electron-donors at the R1 position, which are the key factors for MSOC–CNO (MSOC) and MSNC–CNO (MSNC) possessing large TPA cross sections. In addition, the TPA cross section coming from the electronic transition of  $S_0 \rightarrow S_2$  for MSNC–CNO is dominated by the tensor element  $S_{xx}$ . In the case of MVPC–CNO (MVPC), both tensor elements  $S_{xx}$  and  $S_{xy}$  contribute the TPA cross section for the  $S_0 \rightarrow S_1$  transition, while only  $S_{xx}$  has the major contribution for the  $S_0 \rightarrow S_2$  transition. Obviously, the electronic excitation of  $S_0 \rightarrow S_1$  is assigned primarily to  $\text{HOMO} \rightarrow \text{LUMO}$  (see Table 2), and charge transfer distributes in the  $x$  and  $y$  directions, as shown in Figure S2. However, the electron transition of  $\text{HOMO} \rightarrow \text{LUMO}+1$  is the major configuration for the  $S_0 \rightarrow S_2$  transition, which is associated with intramolecular charge transfer from the donor moiety to 1-methyl-4-vinylpyridium along the  $x$  axis (see Figure S2).

**3.4.4. The Transition Dipole Moment and TPA Tensor Element.** In order to gain insight about the origin of the TPA process, it is helpful to check the various electronic structural parameters and further explore the TPA tensor elements through a few-state model. If the excitation process is contributed mainly by two different states, viz., the ground state and the final state, according to formula 3 in section 2, the TPA tensor element ( $S_{ab}$ ) is expressed as<sup>31,55</sup>

$$S_{ab}^{2\text{SM}} = \frac{2(\mu_a^{0f} \Delta\mu_b + \mu_b^{0f} \Delta\mu_a)}{\omega} \quad (14)$$

Here,  $\mu_a^{0f}$  is the  $a$ th component of the transition dipole moment from the ground to the  $f$  excited state.  $\Delta\mu_a$  is the  $a$ th component of difference between the excited and ground state dipole moments, and  $\omega$  is the excitation energy. These values for reactive products are shown in Table 4. As shown in Table 4, the rules of  $S_{ab}$  are in good agreement with the response theory values (see Table S13) for the studied molecules (except  $S$  for MVPC–CNO). However,  $S_{xx}$  of MVPC–CNO is severely underestimated by the two-state model, which is needed to be expressed in a three-state model,<sup>56</sup> and the quantitative agreement with the response theory value is nearly satisfactory, as shown in Table S14 and Table S15. It is confirmed that there is another important optical channel (the first excited state as an intermediate state) contributed predominantly to the TPA process, and this optical channel is not accounted for in the two-state model for MVPC–CNO.

From Table 4, we can find the following: (1) The change of alkyl chain at the R1 or R2 position is mainly constructive to the enhancement of  $\mu_{xi}$ ; thus,  $S_{xx}$  is larger as the alkyl chain is becoming longer. However, the enhancement of  $S_{xz}$  is in connection with both the transition dipole moment and the difference of dipole moment between two states. (2) The value of  $\Delta\mu_x$  for the cationic compound HC–CNO (−4.94) is much larger than that for the neutral compound HC–N (−1.37); thus, the TPA tensor element  $S_{xx}$  and the TPA cross section ascend dramatically from neutral compound to cationic compound. (3) The strong electron-donors at the R1 position contribute predominantly to  $\Delta\mu$  by improving mainly the

**Table 3.** TPA Tensor Elements ( $S_{ab}$ ) and TPA Cross Sections ( $\delta_{au}$ ) (in au) of All of the Studied Molecules Calculated in Water Solvent<sup>a</sup>

systems	ex. states	TPA tensor elements (in au)						$\delta_{au}$
		$S_{xx}$	$S_{yy}$	$S_{zz}$	$S_{xy}$	$S_{xz}$	$S_{yz}$	
HC–N	1	257.2	−6.9	0.9	66.0	4.2	0.3	425994
HC	1	−528.2	−14.4	−0.4	−135.6	9.9	1.7	1854415
HC–CNO	1	−512.1	−10.8	−0.6	−120.5	−9.0	−1.5	1714386
HCM	1	569.1	4.5	0.5	117.5	8.0	0.9	2065731
HCM–CNO	6	1179.3	26.6	−0.5	−7.5	5.0	0.1	8472454
	1	548.9	1.7	0.7	101.1	7.2	0.8	1895231
HCC	7	1255.6	13.7	−0.6	1.7	7.2	−0.6	9526518
	1	588.4	−3.1	0.8	−97.6	20.0	−2.1	2151367
HCC–CNO	1	566.5	−4.7	1.0	−81.6	18.7	−1.8	1973361
HCB	1	−605.0	13.9	−3.5	54.6	−46.6	2.5	2213292
HCB–CNO	1	−580.2	13.3	−3.5	40.5	−44.2	1.8	2026774
HCH	1	607.8	−17.9	9.4	−16.4	77.5	0.8	2247846
HCH–CNO	6	1201.6	56.6	9.8	193.0	107.6	14.4	9396490
	1	−581.4	15.8	−9.2	4.5	−73.7	−1.6	2057867
	7	1264.5	46.0	11.2	198.6	121.0	18.4	10333961
MBC		594.9	−14.8	1.4	50.2	28.0	−0.4	2119226
MBC–CNO		572.0	−15.0	1.6	28.4	25.9	−0.9	1945540
MSOC	1	721.0	15.4	0.4	−173.8	13.0	−3.6	3409169
MSOC–CNO	1	669.4	27.2	0.5	−186.4	13.3	−4.2	3046759
MSNC	1	867.5	14.4	0.1	157.2	−11.8	−3.7	4765821
MSNC–CNO	2	614.1	39.3	−0.7	6.1	6.4	0.3	2367316
	1	−811.3	−25.1	−0.2	−174.0	12.1	4.2	4278670
MVPC	2	605.8	22.1	−0.9	4.8	7.2	0.6	2256791
	1	202.6	−80.6	1.6	−207.5	5.2	2.5	565453
MVPC–CNO	2	719.2	53.7	−0.9	99.9	2.2	−3.1	3352456
	1	−242.7	74.3	−1.3	233.6	−5.4	−2.2	752122
	2	−705.2	−80.4	1.0	−114.6	0.0	3.4	3351441

<sup>a</sup>Calculations have been done at the CAM-B3LYP/6-31+G(d) level of theory.**Table 4.** Transition Dipole Moments ( $\mu$  in au), the Difference ( $\Delta\mu$ ) of Dipole Moments between the First Excited and Ground States, and TPA Tensor Elements ( $S_{ab}$ ) for the Studied Molecules in Gas Calculated at CAM-B3LYP/6-31+G(d) Using the Gaussian 09 Program

systems	ex. states	$\mu_x^{0f}$	$\mu_y^{0f}$	$\mu_z^{0f}$	$\Delta\mu_x$	$\Delta\mu_y$	$\Delta\mu_z$	$S_{xx}$	$S_{xy}$	$S_{xz}$
HC–N	1	−3.25	−0.38	−0.05	−1.37	−0.33	−0.00	124.93	22.26	1.12
HC–CNO	1	3.99	0.49	0.05	−4.94	0.01	−0.03	−793.33	−48.24	−6.64
HCM–CNO	1	4.17	0.37	0.03	−4.99	0.04	−0.02	−826.86	−32.79	−4.77
HCC–CNO	1	4.24	−0.23	0.10	4.99	0.17	0.11	833.83	−8.46	18.91
HCB–CNO	1	4.31	0.05	0.26	4.99	0.46	0.28	844.90	43.94	48.48
HCH–CNO	1	4.32	0.30	0.45	4.96	0.74	0.48	841.78	91.26	83.72
MBC–CNO	1	4.22	−0.15	0.13	−4.94	0.64	−0.08	−830.82	69.11	−20.05
MSOC–CNO	1	−3.99	1.08	−0.05	−7.76	1.13	−0.07	1360.02	−282.36	14.17
MSNC–CNO	1	3.49	0.64	−0.03	11.22	−0.43	−0.04	1913.27	138.57	−11.21
MVPC–CNO	1	4.24	1.11	−0.05	−0.16	3.24	−0.03	−25.81	252.13	−2.38
	2	−2.07	1.68	0.05	−0.73	3.26	−0.05	49.50	−130.67	2.33

excited state dipole moment (e.g., 3.69 for HCM–CNO and 1.61 for MSOC–CNO). (4) As for MVPC–CNO, the three-state model analysis of  $S^{02}$  reveals a large contribution from the terms involving the S1 state (see Table S14 and Table S15). An excellent TPA cross section and the TPA tensor element, owing to the strong dipole coupling of the virtual state with both the initial and final states, are captured by the transition  $S0 \rightarrow S1 \rightarrow S2$ , with LE–CT mixing transition character. The transition dipole moments  $\mu_x^{01}$  and  $\mu_x^{12}$  have imposed significant impacts on the TPA tensor element  $S_{xx}^{02}$  especially.

In a word, the effect of alkyl chain length on TPA tensor elements, as well as the TPA cross sections, is dominated by the

transition dipole moments  $\mu_x$  for cationic compounds. The difference of TPA cross sections between neutral compound and cationic compound depends on the difference  $\Delta\mu_x$  between the excited and ground state dipole moments mainly. Moreover,  $\Delta\mu_x$  has a major contribution in the two-photon absorption process for the compound with a strong electron-donor at the R1 position. As for the compound with an electron-acceptor at the R1 position, the channel interference effect is obvious.



## 4. CONCLUSIONS

In this work, the geometrical structure, electronic structure, one- and two-photon absorption spectra, and fluorescence properties of a series of carbazole derivatives have been explored in detail by using TDDFT, quadratic response theory, and the few-state model. Calculated results show that there is a little change in spectral properties for the compounds which differ in the length of the alkyl group at the R1 and R2 positions. However, the alkyl chains have an important influence on the fluorescence quantum yield. The relationship between the length of the alkyl chain and the fluorescent quantum yield is not linear for the carbazole derivatives. The compound HCB—CNO with butyl at the R2 position possesses the largest quantum yield (0.485) in all investigated compounds. In addition, the cationic pyridinium moiety not only is the mitochondria-targeted functional group but also plays an important role in geometry relaxation, affecting the optical properties of a compound. As for the fluorescent “off-on” effect, we can conclude that the enhancement of both the electric transition dipole moment and the adiabatic energy between two states of the product as well as the suppression of both the C—N bond stretching and the side-chain bending motions in the low frequency region results in the increased quantum yield after addition of  $\text{ClO}^-$ . It is more important that we clarify the fluorescent quenching mechanism of the probe containing hydroxyl oxime is not from the isomerization of the unbridged C=N bond but is a connection with the increase of both the stretching mode vibration of oxime and the low-frequency motions of the side-chains for all studied reactants for the first time.

Moreover, the effect of introducing electron-donors and -acceptors at R1 positions was studied on OPA and TPA properties. The strong electron-donating groups at the R1 position can lead to pronounced red-shifts of the absorption spectra and a significant increase of TPA cross sections, especially compounds MSOC—CNO (677 GM, 824 nm) and MSNC—CNO (906 GM, 843 nm), which is associated with the large difference of electronic dipole moment between the ground and excited states. However, the molecule MVPC—CNO with a 1-methyl-4-vinylpyridium substituent at the R1 position is not suitable for two-photon fluorescent sensor materials, because of a large geometry change, though it possesses a remarkable TPA cross section (1070 GM, 687 nm). In addition, the proper alkyl chain length is a critical factor for designing high efficiency fluorescent two-photon probes in organisms. A new two-photon fluorescent probe candidate is suggested for detecting hypochlorite in mitochondria and demonstrated the designed compound HCB—CNO displays exceptional optical properties, such as the larger TPA cross section (467 GM) and higher fluorescence quantum yield (0.485), compared with those for experimental molecules. We hope that these results will provide an effective way to design and synthesize a hypochlorite probe with good TP fluorescence behavior based on the carbazole backbone.

## ■ ASSOCIATED CONTENT

### ■ Supporting Information

The Supporting Information is available free of charge on the ACS Publications website at DOI: 10.1021/acs.jpcc.7b10870.

Additional figures and tables (PDF)

## ■ AUTHOR INFORMATION

### Corresponding Author

\*E-mail: [aimin\\_ren@yahoo.com](mailto:aimin_ren@yahoo.com).

### ORCID

Ai-Min Ren: 0000-0002-9192-1483

### Notes

The authors declare no competing financial interest.

## ■ ACKNOWLEDGMENTS

This work is supported by the Natural Science Foundation of China (No. 21173099, 21473071, 20973078, and 20673045) and the Major State Basis Research Development Program (2013CB 834801).

## ■ REFERENCES

- (1) Prokopowicz, Z. M.; Arce, F.; Biedron, R.; Chiang, C. L.; Ciszek, M.; Katz, D. R.; Nowakowska, M.; Zapotoczny, S.; Marcinkiewicz, J.; Chain, B. M. Hypochlorous acid: a natural adjuvant that facilitates antigen processing, cross-priming, and the induction of adaptive immunity. *J. Immunol.* **2010**, *184* (2), 824–35.
- (2) Steinbeck, M. J.; Nesti, L. J.; Sharkey, P. F.; Parvizi, J. Myeloperoxidase and chlorinated peptides in osteoarthritis: potential biomarkers of the disease. *J. Orthop. Res.* **2007**, *25* (9), 1128–35.
- (3) Sugiyama, S.; Kugiyama, K.; Aikawa, M.; Nakamura, S.; Ogawa, H.; Libby, P. Hypochlorous acid, a macrophage product, induces endothelial apoptosis and tissue factor expression: involvement of myeloperoxidase-mediated oxidant in plaque erosion and thrombogenesis. *Arterioscler., Thromb., Vasc. Biol.* **2004**, *24* (7), 1309–14.
- (4) Pattison, D. I.; Davies, M. J. Evidence for rapid inter- and intramolecular chlorine transfer reactions of histamine and carnosine chloramines: implications for the prevention of hypochlorous-acid-mediated damage. *Biochemistry* **2006**, *45* (26), 8152–62.
- (5) Yuan, L.; Wang, L.; Agrawalla, B. K.; Park, S. J.; Zhu, H.; Sivaraman, B.; Peng, J.; Xu, Q. H.; Chang, Y. T. Development of targetable two-photon fluorescent probes to image hypochlorous Acid in mitochondria and lysosome in live cell and inflamed mouse model. *J. Am. Chem. Soc.* **2015**, *137* (18), 5930–8.
- (6) Yue, Y.; Huo, F.; Yin, C.; Escobedo, J. O.; Strongin, R. M. Recent progress in chromogenic and fluorogenic chemosensors for hypochlorous acid. *Analyst* **2016**, *141* (6), 1859–73.
- (7) Xu, Q.; Heo, C. H.; Kim, J. A.; Lee, H. S.; Hu, Y.; Kim, D.; Swamy, K. M.; Kim, G.; Nam, S. J.; Kim, H. M.; Yoon, J. A Selective Imidazoline-2-thione-Bearing Two-Photon Fluorescent Probe for Hypochlorous Acid in Mitochondria. *Anal. Chem.* **2016**, *88* (12), 6615–20.
- (8) Xu, Q.; Heo, C. H.; Kim, G.; Lee, H. W.; Kim, H. M.; Yoon, J. Development of imidazoline-2-thiones based two-photon fluorescence probes for imaging hypochlorite generation in a co-culture system. *Angew. Chem., Int. Ed.* **2015**, *54* (16), 4890–4.
- (9) Xiong, K.; Yin, C.; Chao, J.; Zhang, Y.; Huo, F. The detection for hypochlorite by UV-Vis and fluorescent spectra based on oxidized ring opening and successive hydrolysis reaction. *Spectrochim. Acta, Part A* **2016**, *166*, 79–83.
- (10) Wu, W.-L.; Zhao, Z.-M.; Dai, X.; Su, L.; Zhao, B.-X. A fast-response colorimetric and fluorescent probe for hypochlorite and its real applications in biological imaging. *Sens. Actuators, B* **2016**, *232*, 390–395.
- (11) Wang, X.; Wang, X.; Feng, Y.; Zhu, M.; Yin, H.; Guo, Q.; Meng, X. A two-photon fluorescent probe for detecting endogenous hypochlorite in living cells. *Dalton Trans.* **2015**, *44* (14), 6613–9.
- (12) Li, J.; Yin, C.; Huo, F.; Xiong, K.; Chao, J.; Zhang, Y. Two high selective and sensitive ratiometric fluorescence probes for detecting hypochlorite. *Sens. Actuators, B* **2016**, *231*, 547–551.
- (13) Cheng, T.; Zhao, J.; Wang, Z.; An, J.; Xu, Y.; Qian, X.; Liu, G. A highly sensitive and selective hypochlorite fluorescent probe based on

oxidation of hydrazine via free radical mechanism. *Dyes Pigm.* **2016**, *126*, 218–223.

(14) Zhou, L.; Lu, D. Q.; Wang, Q.; Hu, S.; Wang, H.; Sun, H.; Zhang, X. A high-resolution mitochondria-targeting ratiometric fluorescent probe for detection of the endogenous hypochlorous acid. *Spectrochim. Acta, Part A* **2016**, *166*, 129–134.

(15) Miao, F.; Zhang, W.; Sun, Y.; Zhang, R.; Liu, Y.; Guo, F.; Song, G.; Tian, M.; Yu, X. Novel fluorescent probes for highly selective two-photon imaging of mitochondria in living cells. *Biosens. Bioelectron.* **2014**, *55*, 423–9.

(16) Yang, W.; Chan, P. S.; Chan, M. S.; Li, K. F.; Lo, P. K.; Mak, N. K.; Cheah, K. W.; Wong, M. S. Two-photon fluorescence probes for imaging of mitochondria and lysosomes. *Chem. Commun.* **2013**, *49* (33), 3428–30.

(17) Liu, X.; Sun, Y.; Zhang, Y.; Zhao, N.; Zhao, H.; Wang, G.; Yu, X.; Liu, H. A series of carbazole cationic compounds with large two-photon absorption cross sections for imaging mitochondria in living cells with two-photon fluorescence microscopy. *J. Fluoresc.* **2011**, *21* (2), 497–506.

(18) Zipfel, W. R.; Williams, R. M.; Webb, W. W. Nonlinear magic: multiphoton microscopy in the biosciences. *Nat. Biotechnol.* **2003**, *21* (11), 1369–77.

(19) Helmchen, F.; Denk, W. Deep tissue two-photon microscopy. *Nat. Methods* **2005**, *2* (12), 932–40.

(20) Williams, R. M.; Zipfel, W. R.; Webb, W. W. Multiphoton microscopy in biological research. *Curr. Opin. Chem. Biol.* **2001**, *5* (5), 603–8.

(21) Kim, H. M.; Cho, B. R. Small-molecule two-photon probes for bioimaging applications. *Chem. Rev.* **2015**, *115* (11), 5014–55.

(22) Liu, H. W.; Liu, Y.; Wang, P.; Zhang, X. B. Molecular engineering of two-photon fluorescent probes for bioimaging applications. *Methods Appl. Fluoresc.* **2017**, *5* (1), 012003.

(23) Li, D.; Feng, Y.; Lin, J.; Chen, M.; Wang, S.; Wang, X.; Sheng, H.; Shao, Z.; Zhu, M.; Meng, X. A mitochondria-targeted two-photon fluorescent probe for highly selective and rapid detection of hypochlorite and its bio-imaging in living cells. *Sens. Actuators, B* **2016**, *222*, 483–491.

(24) Chi, S.; Li, L.; Wu, Y. A series of novel dibenzothiophene-based two-photon fluorescent probes for cellular nucleus imaging. *Sens. Actuators, B* **2016**, *231*, 811–829.

(25) Kim, H. M.; Kim, B. R.; Choo, H. J.; Ko, Y. G.; Jeon, S. J.; Kim, C. H.; Joo, T.; Cho, B. R. Two-photon fluorescent probes for biomembrane imaging: effect of chain length. *ChemBioChem* **2008**, *9* (17), 2830–8.

(26) Wu, J.; Liu, W.; Ge, J.; Zhang, H.; Wang, P. New sensing mechanisms for design of fluorescent chemosensors emerging in recent years. *Chem. Soc. Rev.* **2011**, *40* (7), 3483–95.

(27) Cheng, X.; Jia, H.; Long, T.; Feng, J.; Qin, J.; Li, Z. A “turn-on” fluorescent probe for hypochlorous acid: convenient synthesis, good sensing performance, and a new design strategy by the removal of C=N isomerization. *Chem. Commun.* **2011**, *47* (43), 11978–80.

(28) Emrullahoglu, M.; Ucuncu, M.; Karakus, E. A BODIPY aldoxime-based chemodosimeter for highly selective and rapid detection of hypochlorous acid. *Chem. Commun.* **2013**, *49* (71), 7836–8.

(29) Padwa, A. Photochemistry of the Carbon-Nitrogen Double Bond. *Chem. Rev.* **1977**, *77*, 37.

(30) Peticolas, W. L. Multiphoton spectroscopy. *Annu. Rev. Phys. Chem.* **1967**, *18* (1), 233–260.

(31) Beerepoot, M. T.; Friese, D. H.; List, N. H.; Kongsted, J.; Ruud, K. Benchmarking two-photon absorption cross sections: performance of CC2 and CAM-B3LYP. *Phys. Chem. Chem. Phys.* **2015**, *17* (29), 19306–14.

(32) Rudberg, E.; Salek, P.; Helgaker, T.; Agren, H. Calculations of two-photon charge-transfer excitations using Coulomb-attenuated density-functional theory. *J. Chem. Phys.* **2005**, *123* (18), 184108.

(33) Monson, P. R.; McClain, W. M. Polarization Dependence of the Two-Photon Absorption of Tumbling Molecules with Application to

Liquid 1-Chloronaphthalene and Benzene. *J. Chem. Phys.* **1970**, *53* (1), 29–37.

(34) Friese, D. H.; Beerepoot, M. T.; Ruud, K. Rotational averaging of multiphoton absorption cross sections. *J. Chem. Phys.* **2014**, *141* (20), 204103.

(35) Aidas, K.; Angeli, C.; Bak, K. L.; Bakken, V.; Bast, R.; Boman, L.; Christiansen, O.; Cimiraglia, R.; Coriani, S.; Dahle, P.; et al. The Dalton quantum chemistry program system. *Wiley Interdiscip. Rev. Comput. Mol. Sci.* **2014**, *4* (3), 269–284.

(36) Niu, Y. L.; Peng, Q. A.; Deng, C. M.; Gao, X.; Shuai, Z. G. Theory of Excited State Decays and Optical Spectra: Application to Polyatomic Molecules. *J. Phys. Chem. A* **2010**, *114* (30), 7817–7831.

(37) Santoro, F.; Lami, A.; Improta, R.; Bloino, J.; Barone, V. Effective method for the computation of optical spectra of large molecules at finite temperature including the Duschinsky and Herzberg-Teller effect: the Q<sub>x</sub> band of porphyrin as a case study. *J. Chem. Phys.* **2008**, *128* (22), 224311.

(38) Niu, Y.; Peng, Q.; Shuai, Z. Promoting-mode free formalism for excited state radiationless decay process with Duschinsky rotation effect. *Sci. China, Ser. B: Chem.* **2008**, *51* (12), 1153–1158.

(39) Englman, R.; Jortner, J. The energy gap law for radiationless transitions in large molecules. *Mol. Phys.* **1970**, *18* (2), 145–164.

(40) Lin, S. H. Rate of Interconversion of Electronic and Vibrational Energy. *J. Chem. Phys.* **1966**, *44* (10), 3759–3767.

(41) Shuai, Z.; Peng, Q.; Niu, Y.; Geng, H. MOMAP, revision 0.3.001; Beijing, China, 2016 (MOMAP: a free and open-source molecular materials property prediction package; available online at: <http://www.shuaigroup.net>).

(42) Frisch, M. J.; Trucks, G. W.; Schlegel, H. B.; Scuseria, G. E.; Robb, M. A.; Cheeseman, J. R.; Scalmani, G.; Barone, V.; Mennucci, B.; Petersson, G. A.; et al. *Gaussian 09*, revision D.01; Gaussian, Inc.: Wallingford, CT, 2009.

(43) Laurent, A. D.; Jacquemin, D. TD-DFT benchmarks: A review. *Int. J. Quantum Chem.* **2013**, *113* (17), 2019–2039.

(44) Yanai, T.; Tew, D. P.; Handy, N. C. A new hybrid exchange–correlation functional using the Coulomb-attenuating method (CAM-B3LYP). *Chem. Phys. Lett.* **2004**, *393* (1–3), 51–57.

(45) Paterson, M. J.; Christiansen, O.; Pawłowski, F.; Jorgensen, P.; Hattig, C.; Helgaker, T.; Salek, P. Benchmarking two-photon absorption with CC3 quadratic response theory, and comparison with density-functional response theory. *J. Chem. Phys.* **2006**, *124* (5), 054322.

(46) List, N. H.; Zalesny, R.; Murugan, N. A.; Kongsted, J.; Bartkowiak, W.; Agren, H. Relation between Nonlinear Optical Properties of Push-Pull Molecules and Metric of Charge Transfer Excitations. *J. Chem. Theory Comput.* **2015**, *11* (9), 4182–8.

(47) Salek, P.; Vahtras, O.; Helgaker, T.; Ågren, H. Density-functional theory of linear and nonlinear time-dependent molecular properties. *J. Chem. Phys.* **2002**, *117* (21), 9630–9645.

(48) Tomasi, J.; Mennucci, B.; Cammi, R. Quantum mechanical continuum solvation models. *Chem. Rev.* **2005**, *105* (8), 2999–3093.

(49) Weber, P.; Reimers, J. R. Ab initio and density-functional calculations of the vibrational structure of the singlet and triplet excited states of pyrazine. *J. Phys. Chem. A* **1999**, *103* (48), 9830–9841.

(50) Cai, Z. L.; Reimers, J. R. The low-lying excited states of pyridine. *J. Phys. Chem. A* **2000**, *104* (36), 8389–8408.

(51) Dumat, B.; Bordeaux, G.; Faurel-Paul, E.; Mahuteau-Betzer, F.; Saettel, N.; Bomble, M.; Metge, G.; Charra, F.; Fiorini-Debuisschert, C.; Teulade-Fichou, M. P. N-phenyl-carbazole-based two-photon fluorescent probes: strong sequence dependence of the duplex vs quadruplex selectivity. *Biochimie* **2011**, *93* (8), 1209–18.

(52) Peng, Q.; Yi, Y.; Shuai, Z.; Shao, J. Toward quantitative prediction of molecular fluorescence quantum efficiency: role of duschinsky rotation. *J. Am. Chem. Soc.* **2007**, *129* (30), 9333–9.

(53) McClain, W. M. Excited State Symmetry Assignment Through Polarized Two-Photon Absorption Studies of Fluids. *J. Chem. Phys.* **1971**, *55* (6), 2789–2796.

(54) Alam, M. M.; Chattopadhyaya, M.; Chakrabarti, S. Solvent induced channel interference in the two-photon absorption process—a

theoretical study with a generalized few-state-model in three dimensions. *Phys. Chem. Chem. Phys.* **2012**, *14* (3), 1156–65.

(55) Murugan, N. A.; Zalesny, R.; Kongsted, J.; Nordberg, A.; Agren, H. Promising two-photon probes for in vivo detection of beta amyloid deposits. *Chem. Commun.* **2014**, *50* (79), 11694–7.

(56) Nanda, K. D.; Krylov, A. I. Visualizing the Contributions of Virtual States to Two-Photon Absorption Cross Sections by Natural Transition Orbitals of Response Transition Density Matrices. *J. Phys. Chem. Lett.* **2017**, *8* (14), 3256–3265.